Journal of Materials Chemistry A

Accepted Manuscript

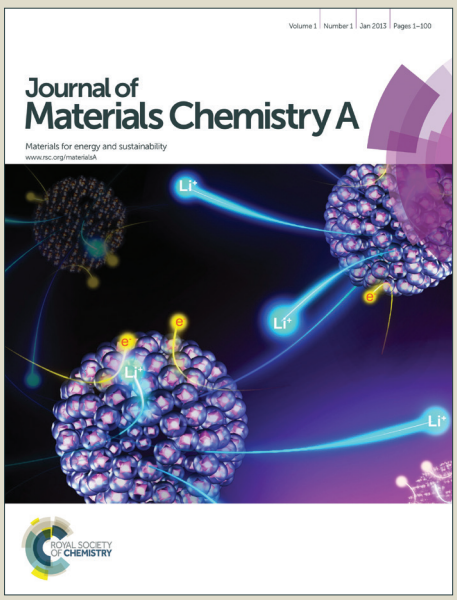

ROYAL SOCIETY OF CHEMISTRY

www.rsc.org/materialsA

Cite this: DOI: 10.1039/c0xx00000x

www.rsc.org/xxxxxx

ARTICLE TYPE

Electrochemical Nucleation and Growth of Pd/PdCo Core – Shell Nanoparticles with Enhanced Activity and Durability as Direct Formic Acid Fuel Cell Catalyst

MiladRezaei,[a]Seyed Hadi Tabaian,*[a]and Davoud Fatmehsari Haghshenas[a]

Received (in XXX, XXX) XthXXXXXXXXX 20XX, Accepted Xth XXXXXXXXX 20XX
DOI: 10.1039/b000000x

This work presents an innovative approach for the preparation of a promising nano-sized catalyst, the Pd/PdCo core-shell nanoparticles (NPs), with an enhanced catalytic activity and durability for formic acid electro-oxidation. By addressing the kinetics of nucleation during electrodeposition we developed a method for synthesizing Pd/PdCo core-shell NPs with a shell thickness of ca. 2 nm. During initial times of step potential electrodeposition, Pd deposited as the core due to higher nucleation rate of Pd compared to Co and then, the co-electrodeposition of Pd and Co leads to formation of a thin PdCo shell. The results of formic acid (FA) electro-oxidation by the synthesized Pd/PdCo core-shell NPs revealed a mass activity of 1580 mA/mg_{Pd} at the peak potential which is three times higher than that of Pd NPs (j_P=540 mA/mg_{Pd}). Based on the X-ray photoelectron spectroscopy (XPS), the mechanistic origin of the variation in activity and durability was attributed to the change of electronic band structure of Pd/PdCo core-shell which resulted in the weakening chemisorption of intermediate anion species. The material synthesized herein is a promising catalyst for fuel cell applications and the facile synthesis method can be readily adapted to other core-shell catalyst systems, facilitating screening of high efficiency catalysts.

Introduction

During recent years, many efforts have been devoted to electrodeposition of Pd-based bimetallic catalysts for the proton exchange membrane fuel cells (PEMFCs).[1-4] The major reason for this issue is that the catalytic activity of the Pd increases notably in the presence of some metals such as Co, Fe, and Ni and thus, there can be some reasonable alternatives for Pt based catalysts in PEMFCs.[3-11] In the electrodeposition process of the bimetallic systems, the main complexity is due to the nucleation and growth of two components which must be correctly identified and controlled during process; the careful monitoring and controlling of the system is necessary for achieving the favorable degree of alloying[1] as well as the proper structure.[2]

There is an extensive literature on the nucleation mechanisms during electrodeposition process of the bimetallic systems; among these works, some investigators have obtained the kinetic information by the use of simple models.[2,12-15] On the other hand, Milchev et al. have employed the atomistic theory of nucleation for a comprehensive description of the early stage of alloy nucleation. They have also developed a method for quantification of the size and composition of critical alloy nuclei by the evaluation of potential and concentration dependence of the stationary nucleation rate.[16,17] Recently, a mathematical expression for the current transients has been derived from the experimental current transients under potentiostatic conditions.[18] This mathematical expression can well describe the kinetics of nucleation and diffusion-controlled growth of bimetallic clusters and consequently, the number density of active sites (N_0) and nucleation frequency (A) have been estimated as the kinetic information. However, this valuable mathematical expression is only valid in the systems which the thermodynamic characteristics of the components are very similar such as Hg-Ag with near standard redox potential.[18] Thus, in bimetallic systems composed of "Pd-transition metal", this model is inapplicable.[12,18]

In the present work, we attempt to present a semi-empirical model for the evaluation/description of palladium-cobalt co-electrodeposition process. In this regards, first the electrochemical nucleation and growth of Pd on the carbon cloth is evaluated using current-time transient (CTT) step potential technique. The contribution of hydrogen co-reduction process is determined and, the variation of CTT in the presence of Co (II) is studied. By identification of the contributions of Pd, H and Co reduction processes and presumption the nucleation mechanisms, the verification of the mechanisms is carried out by the experimental evidences such as high-resolution transmission electron microscopy (HRTEM), electron energy loss spectroscopy (EELS), X-ray diffractometry (XRD) and X-ray photoelectron spectroscopy (XPS). These evidences provide some clues regarding the formation of a thin PdCo alloy shell around the primary nucleated Pd core during the electrodeposition process. Finally, the catalytic performance of

Pd/PdCo core-shell nanoparticles, electrodeposited Pd nanoparticles and commercial Pd/C catalysts are compared in formic acid electro-oxidation process.

Experimental

Preparation of the catalyst electrodes: Before each experiment, the carbon cloth (TGPH-090 Toray) was immersed for a minute in nitric acid solution to remove any impurity from its surface, and then washed carefully with acetone and distilled water. 1 cm^2 of carbon cloth (CC), as working electrode, was exposed to the solution and other conducting parts were sealed with a PTFE holder. A platinum plate and an Ag/AgCl were used as the counter and reference electrodes, respectively. The electrolytes composition were i) 50 mM $CoSO_4$ + 1 M NH_4Cl, ii) 10 mM $PdCl_2$ + 1 M NH_4Cl and iii) 10 mM $PdCl_2$ + 50 mM $CoSO_4$ + NH_4Cl. All electrochemical experiments were conducted in a conventional three-electrode electrochemical cell at 25 ^oC using a potentiostat/galvanostat Autolab® PGSTAT 30. In order to obtain the current transient curves during Pd and PdCo nanoparticles electrodeposition, the open circuit potential (OCP) was applied for initial 60 s and, thereafter, the value of applied potential was brought down to –1.2 V. After electrodeposition, the electrode was rinsed with ultrapure water to remove any residue of precursors that may degrade the electro-catalyst performance. For comparison purposes, the commercial Pd/C (Pd weight ratio of 20% supported on Vulcan XC-72R) was suspended in Nafion solution (5 wt. %) and spread on carbon cloth to prepare a standard catalyst electrode (Pd loading = 0.3 mg cm^{-2}).

Physical analysis: The morphology and size of the electrodeposited nanoparticles were characterized by field emission scanning electron microscopy (FESEM) using a MIRA-TESCAN equipped with an energy dispersive X-ray spectrometer (EDAX DX-4) and transmission electron microscopy (TEM) using a FEI Titan 50-300 equipment.

The crystallographic structures of metal NPs were analysed by X-ray diffractometry (XRD-EQuinox 3000) with a Cu K_α (λ=1.54 Å) source.

X-ray photoelectron spectroscopy (XPS) was carried out by a Thermo VG Scientific ESCALAB 250 spectrometer with Al K_α radiation (hυ = 1486.6 eV). The binding energies were referenced to C 1s peak at 284.6 eV.

In order to determine the amount of Pd catalyst loading, the deposited nanoparticles were removed from the substrate by a 3:1 mixture of HCl and HNO_3 (aqua regia) and the obtained solution was analyzed by an UV-visible spectrophotometer (UNICAM 8700) based on the Lambert-Beer law.

The electron energy loss spectroscopy (EELS) was performed in a FEI Titan 50–300 electron microscope operated at 80 kV. The EELS spectra were recorded with a Quantum ERS system analyzing. The energy resolution was ~ 1 eV which determined from the full-width at half-maximum of the zero-loss peaks. For the EELS line profile measurements, both Co L-edge and Pd M-edge spectra were collected along about 40 points across a nanoparticle with an acquisition time of 2 s per spectrum.[6,19]

Catalytic characterizations: Cyclic voltammetry (CV) and chronoamperometry (CA) were employed to examine the catalytic activity and durability of the Pd NPs (deposition time = 15 s in solution (ii)) and Pd/PdCo core-shell NPs (deposition time = 15 s in solution (iii)) catalysts for formic acid oxidation in a solution of 0.5 M formic acid and 0.5 M sulfuric acid. The electrolyte solution was purged thoroughly with pure nitrogen prior to each experiment to remove any dissolved oxygen. The CVs were repeated till a reproducible curve was acquired. The active surface area of the catalysts was determined from the blank voltammograms. It was conducted by measuring the charge involved in the so-called hydrogen adsorption/desorption ((Q_{ads}+Q_{des})/2) region between –0.2 and 0.15 V (vs. Ag/AgCl) and assuming 210 μC cm^{-2} for the total charge corresponding to the adsorption of a monolayer of hydrogen on a polycrystalline Pd surface in N_2 deaereated 0.5 M sulfuric acid solutions.[8,20,21] Membrane electrode assemblies (MEAs) were prepared using Pd/C, electrodeposited Pd and Pd/PdCo core-shell NPs as the anodes, Nafion 115 membrane (DuPont Inc.), and commercial gas diffusion electrodes (10 wt. % Pt/C, 0.2 mg cm^{-2}, Johnson Matthey) as the cathodes. The electrodeposited Pd and Pd/PdCo core-shell NPs were painted with 5 wt. % Nafion solution to obtain a Nafion loading of ≃ 0.1 mg cm^{-2} on each electrode. The Nafion-impregnated electrodes and membrane were then hot pressed together at 120^{o}C for 3 min under a pressure of 120 atm to form the MEA. Subsequently, the MEA was inserted between two graphite plates which had a serpentine flow pattern. The performance test was conducted using a 5 cm^2 single fuel cell operated at room temperature. The formic acid aqueous solution (0.5 M) was delivered to the anode with a rate of 1 ml min^{-1}, and the air was spontaneously diffused to cathode as the oxidant. The Fuel cell performance (polarization curves) was evaluated at room temperature under atmospheric pressure using a potentiostat/galvanostat Autolab® PGSTAT 30.

Results and Discussion

Potentiodynamic behavior of Pd(II) and Co(II): Fig. 1a illustrates the electrochemical behavior of carbon cloth in three distinct solutions; i) 50 mM $CoSO_4$ (pH≃3.5), ii) 10 mM $PdCl_2$ (pH≃3.4) and iii) 10 mM $PdCl_2$ + 50 mM $CoSO_4$ (pH≃3.2) in the presence of 1 M NH_4Cl as the electrolyte supporting. In voltammogram corresponding to solution (i), small currents (close to zero) are detected in the negative sweep at the potentials more positive than the cobalt reduction potential (–950 mV), followed by a further increase in the current which is due to water decomposition (hydrogen reduction). The current remains cathodic until the reversion of sweep towards the positive potentials; where at –620 mV, it crosses over the current recorded during negative sweep. This current loop (shown as region "A" in Fig. 1a) is due to the fact that the overpotential for the deposition of a metal onto its own (in this case cobalt on cobalt) is lower than that for the deposition of metal onto different substrates (in this case cobalt on CC). This phenomenon is frequently observed in cyclic voltammograms when nucleation processes are involved.[22] The anodic peak observed at +200 mV (peak "B" in Fig. 1a) is ascribed to the dissolution of deposited Co in the form of $[CoCl]^+$ as the predominant ionic complex at this pH range (Fig. S1).

In the case of solution (ii), the voltammogram reveals that during forward scan toward negative potentials, the cathodic current

increases sharply once Pd nucleation begins. The sharp increase in the cathodic current at the peak potentials of –0.15 V (peak "D" in Fig. 1a) indicates the diffusion-controlled reduction of Pd.[23] Another cathodic current peak is observed in the potential about –600 mV (peak "E" in Fig. 1a) which is the characteristic of hydrogen adsorption onto the Pd particles.[24] On the reverse scan and after the anodic peaks related to the hydrogen oxidation and/or desorption processes (peak "F"), an anodic current peak (peak "G") appears at E ~ 850 mV which is assigned to the oxidation of Pd particles to $[PdCl_4]^{2-}$.

Figure 1

In the case of $PdCl_2$ + $CoSO_4$ mixture (solution (iii)), the recorded CV shows a hybrid behavior; As it can be seen in Fig. 1a, two peaks "H" and "I" are the same as the peaks observed for solution (ii) which can assigned to $[PdCl_4]^{2-}$ reduction and hydrogen adsorption, respectively. Compared to solution (ii), the voltammogram corresponding to solution (iii) has a sharper slope at the end of cathodic scan (Fig. 1b) indicating co-deposition of cobalt.[2] At the reverse anodic scan, a distinctive wide peak (peak "J") is observed which, according to Fig. 1b, is attributed to two consecutive and/or simultaneous processes; hydrogen desorption[24] and cobalt dissolution.[25]

The shape of Pd dissolution peak (peak "K") is slightly different from the pure Pd dissolution (peak "G"). While the end limit of peak "K" completely matches to peak "G" (see Fig. 1b), its first part initiates at lower potentials than peak "G". It seems that peak "K" is consisted of two anodic peaks as shown by arrows in Fig. 1b.This behavior may be due to primary dissolution of partially alloyed Pd and then dissolving of pure residual Pd.

Nucleation Mechanisms: In order to study the initial stages of Pd nanoparticles formation, the transient of CC electrode recorded at potential of –1.2 V in solution (ii) (1 M NH_4Cl + 10 mM $PdCl_2$) is shown in Fig. 2a. As is depicted in the inset of Fig. 2a, there is an initial decay in the current transient curve which is maybe the result of $[PdCl_4]^{2-}$ ions adsorption stage (i.e. charging of an adsorption pseudo-capacitance); subsequently, there is a rapid rise in the curve up to a peak where is again followed by a gradual decay toward a nonzero limiting value. This general trend in the transient curve indicates the occurrence of nucleation and growth stages during the process.[22,26,27] Since the potential of system is in the range of hydrogen reduction potential (Fig. S1) and regarding the modified surface of CC by Pd nuclei, which is a very favorable catalyst for the hydrogen reduction, it is expected that hydrogen simultaneously reduces during Pd electrodeposition.[24] Therefore, the current-time curve consists of three parts corresponding to (i) the current transient due to the charging of an adsorption pseudo-capacitance, (ii) Pd nucleation and growth and (iii) hydrogen reduction which occurs on the surface of interacting growing palladium nuclei. For quantitative description of the current transient, all these three terms should be taken into account as:[25]

$$j=\overbrace{k_1\exp(-k_2t)}^{(i)}+[\overbrace{\frac{zFD^{1/2}C}{\pi^{1/2}t^{1/2}}}^{(ii)}+\overbrace{\sqrt{\frac{2}{\pi}}z_HFk_HC^{1/2}V_m^{1/2}}^{(iii)}]\times [1-\exp(-2\sqrt{2}\pi^{3/2}N_0C^{1/2}V_m^{1/2}Dt\theta)] \quad (1)$$

where $k_1 = k_2 \times q_{Ads}$ and q_{Ads} is the total charge density due to the adsorption process; The moles of transferred electrons in the hydrogen reduction reaction and the rate constant of this reaction are shown by z_H and k_H, respectively. Also, zF, D, C, N_0 and V_m are the molar charge transferred during electrodeposition, Pd diffusion coefficient, bulk concentration of the electrolyte, the number of active sites and molar volume of the deposit, respectively. Moreover, the relation between θ and time is $\theta=1-(1-\exp(-At))/At$ in which A is the nucleation rate constant. By the use of Eq. (1), the mathematical fitting procedure of the experimental data was conducted; the deconvoluted transients corresponding to adsorption, Pd nucleation and hydrogen co-reduction are presented in Fig. 2a.

Figure 2

In addition, the constants of Eq. (1), derived from the fitting procedure, are listed in Table 1. The predicted diffusion coefficient ($D=6.1\times10^{-5}$ cm^2s^{-1}) has a good compatibility with those reported in the literature [2,13,22-24] indicating the applicability of the fitting procedure.[25] In the case of Co (solution (i)), same procedure was applied and the results are given in Fig. S2.

Table 1: The constants of Eq. (1) corresponding to simultaneous adsorption of the $[PdCl_4]^{2-}$, Pd nucleation and growth and reduction of hydrogen

k_1 (A cm^{-2})	k_2 (s^{-1})	N_0 (cm^{-2})	D (cm^2 s^{-1})	A (s^{-1})	k_H (mol cm^{-2} s^{-1})
0.045	2.88	$1.7\times10^{+7}$	6.1×10^{-5}	1.01	0.9×10^{-5}

As it is observed in Fig. 2b, at the initial times (t < 5.1 s) the experimental current transients corresponding to Pd (solution (ii)) and Pd-Co (solution (iii)) are similar at E= –1.2. However, this similarity ends after ≃5.1 s. Accordingly, it is likely that only Pd nuclei are formed at the initial times (t < 5.1 s) of deposition and, the co-deposition of Pd and Co starts after 5.1 s. This conclusion was approved by the results of micrographs as well as the EDS analysis (Fig. 3a-d) corresponding to the nanoparticles obtained after 4 and 15 s of deposition in solution (iii). The presence of only Pd (appearance of L_α=2.838 and L_β=2.913 KeV) peaks beside the absence of Co (non-appearance of L_α=0.776, K_α=6.924 and K_β=7.649 KeV) peaks reveals that at the initial times of deposition only Pd nucleates (or at least Co nucleation is so negligible).

Figure 3

In order to shed more lights on the structure of the deposited nanoparticles (deposited for 15 seconds), the corresponding HRTEM micrograph, elemental color-map and line profiles are presented in Fig. 4a-c which shows that Pd has been confined in the center of nanoparticle and a thin Pd-Co layer covers the surface of Pd core.

Figure 4

In summary, the nucleation mechanisms of Pd/PdCo core-shell can be regarded as the initial formation of hemispherical Pd nuclei in which they serve as the favorable sites for following palladium and cobalt deposition; in other words, after a primary induction time (ca. 5.1 s, according to PdCo transient in Fig. 2b), the reduction of cobalt ions over the pre-nucleated/pre-grown Pd nanoparticles starts resulting in the co-deposition of palladium and cobalt. During this co-reduction process, cobalt atoms may be incorporated into the palladium structure (alloy formation) which can be examined by XRD analysis.

Crystal Phases and Electronic Structure: Fig. 5a shows XRD patterns corresponding to Pd (electrodeposited for 15 s in solution

(ii)) and Pd/PdCo (electrodeposited for 15 s in solution (iii)) catalysts. The structural patterns of catalysts indicate a face centered cubic (fcc) structure for both catalysts. It is worthy of note that general feature of the diffraction pattern corresponding to Pd/PdCo catalyst is similar to that of Pd catalyst; however, the diffraction peaks center were shifted toward higher angles in the case of Pd/PdCo catalyst which can be ascribed to the compression in lattice crystal of Pd for adopting Co structure during co-electrodeposition process. The incorporation of Co into Pd structure can effectively modify Pd electronic structure. However, to monitor the chemical changes and electronic structure of the nanoparticles surface, the XPS technique should be employed.

The X-ray photoelectron spectrum (XPS) of Pd/PdCo core-shell (deposited for 15 s in solution (iii)) is shown in Fig. 5b. The main peaks observed in quick survey scan are related to Pd 3d, Pd 3p, Co 2p, C 1s, and O 1s. The relative Co:Pd atomic percentage at the surface of Pd/PdCo core-shell nanoparticles is estimated to be 25.1:74.9, slightly higher than that obtained from EDS measurement (22.4:77.6, Fig. 3d). In order to acquire a better understanding of the chemical nature and electronic structure of the obtained structure, a critical comparison between Pd $3d_{5/2}$ and $3d_{3/2}$ detailed regions of the 4 s deposited NPs (including only Pd) and 15 s deposited NPs (the Pd nuclei surrounded by a thin PdCo shell) was made (Fig. 5c). In the case of Pd NPs, the binding energy for $3d_{5/2}$ peak (335.2) is 0.1 eV higher than that of standard bulk metallic Pd (335.1 eV).[28] This positive shift may be attributed to the final state relaxation (particle size effect).[29] It should be noted that the standard binding energies of Pd oxides are 336.3 eV (PdO) and 337.9 eV (PdO_2).[28] By deconvolution of the Pd 3d peaks to Pd^0 and Pd^{II} besides the relative peak areas measurements, the percentage of Pd^0 species is calculated to be 67.1% indicating that Pd is predominately in metallic state together with some surface oxides. However, the corresponding peak ($3d_{5/2}$) to the Pd/PdCo core-shell NPs, shifts to lower binding energy ($\Delta E \sim -0.5$ eV) compared to Pd NPs. This can be elucidated in terms of the electronic effect of Co on Pd. This shift of binding energy is due to the slight electron transfer from Co to Pd,[29] consistent with the difference in the electronegativity of Pd and Co (Pd=2.20 and Co=1.88).[30] Therefore, the addition of Co produces an electronic effect due to incorporating into the Pd structure. However, the shift in Pd/PdCo core-shell NPs binding energy (–0.5 eV) is more than the shift in completely alloyed PdCo (–0.29 eV[31]) implying surface electronic modification of the PdCo shell resulting from the interaction with the Pd core.[32] By measuring the relative peak areas, the percentage of Pd^0 species in the PdCo shell, is 85.4%, much higher than that in the Pd core (67.1%), indicating the oxide-cleansing action of this structure[29-31] that expected to enhance the catalytic activity of Pd for electro-oxidation reactions involves several intermediates. In fact, the PdCo shell have a lower tendency to adsorb the reactive intermediate compared to Pd due to the downshift in d-band center in agreement with the prediction of d-band center theory which states by lowering the d-band center, the interaction strength of the adsorbents to the catalyst surface decreases.[29-33]

Figure 5

Electro-oxidation of Formic Acid: The catalytic performance of commercial Pd/C (20 wt. %), electrodeposited Pd NPs (deposition time = 15 s in solution (ii)) and Pd/PdCo core-shell NPs (deposition time = 15 s in solution (iii)) catalysts in 0.5 M H_2SO_4 + 0.5 M HCOOH, normalized against mass of Pd, is presented in Fig. 6a. In the positive scan direction, the mass activity of the Pd/PdCo core-shell NPs at peak potential reaches to 1.580 A mg^{-1}, which is about 3 and 5 times higher than those corresponding to Pd NPs (0.540 A mg^{-1}) and Pd/C (0.325 A mg^{-1} which shows a satisfied compatibility to those reported previously[30-32]), respectively; this indicates that the Pd loading can be effectively reduced by using Pd/PdCo core-shell NPs as the anode catalysts in DFAFC. Furthermore, the peak potential (E_P) of the FA oxidation corresponding to Pd/PdCo core-shell NPs negatively shifts (~ 70 mV) compared to the Pd NPs. In the case of Pd/C and Pd NPs, the first current maximum in the forward scan is due to the direct oxidation of HCOOH to CO_2 (dehydrogenation reaction),[34,35] while the second current maximum is because of CO oxidation generated from the dehydration reaction of HCOOH as mentioned below:[31,35]

Dehydrogenation:

$$Pd+HCOOH \rightarrow Pd\text{-}HCOO_{ads}+H^+ +e \quad (2)$$

$$Pd\text{-}HCOO_{ads} \rightarrow Pd+CO_2+H^+ +e \quad (3)$$

Dehydration:

$$Pd+HCOOH \rightarrow Pd\text{-}HCOO_{ads}+H^+ +e \quad (4)$$

$$Pd\text{-}HCOO_{ads}+2(Pd\text{-}H_{ads}) \rightarrow Pd\text{-}HCO_{ads}+H_2O \quad (5)$$

$$Pd\text{-}HCO_{ads} \rightarrow Pd\text{-}CO_{ads}+H^+ +e \quad (6)$$

Therefore, if the FA Electro-oxidation reaction does not proceed only through the dehydrogenation pathway, CO can act as one of the major reactive intermediates.[34] However, no oxidation peak (corresponding to CO oxidation) is observed at Pd/PdCo core-shell NPs voltammogram indicating that PdCo shell surface promotes the dehydrogenation reaction of HCOOH and inhibits the dehydration reaction; i.e. FA electro-oxidation solely proceeds via the direct pathway on the surface of Pd/PdCo core-shell NPs.

Without the CO-poisoning effect, the Pd/PdCo core-shell NPs have an onset FA oxidation potential at $E_S = -198$ mV, which is lower than that of Pd NPs (–173 mV) and Pd/C (–169 mV), respectively. The quantitative catalytic performance obtained for Pd/C, electrodeposited Pd and Pd/PdCo core-shell NPs catalysts are summarized in Table 2.

Table 2: The quantitative catalytic properties of a commercial Pd/C (20 wt. %), electrodeposited Pd NPs and Pd/PdCo core-shell NPs.

	j_P[a]	$j_{@E=0.2\,V}$[a]	E_P[a]	E_S[a]	$\frac{j_f}{j_b}$[a]	CO peak[a]	$\frac{j\ @\ t=40{,}000s}{j\ @\ t=20s}$[b]	ECSA[c]
	A/mg_{Pd}	A/mg_{Pd}	mV	mV				m^2/gr
Pd/C	0.325	0.309	141	-169	1.14	Yes	11.1%	47.1
Pd NPs	0.540	0.326	486	-173	1.32	Yes	16.4%	62.9
Pd/PdCo	1.580	0.969	416	-198	1.76	No	40.6%	66.7

[a]derived from Fig. 6a,[b]derived from Fig. 6b,[c]derived from Fig. S3.

Figure 6

In fact, for successful production of a Pd based catalyst with an effective electrocatalytic performance for the FA oxidation, the catalyst should counterbalance two opposing effects: i) a relatively strong adsorption energy of FA and reaction intermediates and ii) a relatively low coverage by spectator adsorbed anions (e.g., formate ions).[33] Therefore, for metal surfaces that bind anions too strongly, the rate of FA oxidation

reaction is limited by the availability of anion-free Pd sites. On the other hand, where the surface is less covered by anions, but the adsorption energy of the intermediates (formate) is too low to enable a high rate of the FA oxidation. Therefore, if a catalyst binds formate too strongly, the rate will be limited by the rate of removing surface formate and when a catalyst binds formate too weakly, the rate would be limited by the rate of electron and proton transfer from adsorbed formate (reaction 3).[36] Accordingly, FA oxidation rate via dehydrogenation pathway is expressed as:[36,37]

$$j = nFKC_{FA}(1-\theta_{ads})^{x}\exp(-\beta FE/RT)\exp(-\gamma\Delta G_{ads}/RT) \qquad (7)$$

in which n, F, K, C_{FA} ,R ,x ,β and γ are constants, E is the electrode potential, T is the temperature and θ_{ads} is the total surface coverage by formate ions and ΔG_{ads} is the Gibbs energy of adsorption of formate. Eq. (7) indicates that, both the lower θ_{ads} and the more negative ΔG_{ads} are necessary to increase the activity of catalyst. Although alloying Pd with a transition metal such as Co can provide the first condition[33,36] but the second one will not be necessarily satisfied.[37] However a fine Pd core surrounded by a thin PdCo shell may provide both conditions simultaneously which will be more discussed in the next section (catalyst stability).

The poisoning tolerance (j_f/j_b), defined as the ratio of peak current in the forward scan (j_f) to peak current in backward scan (j_b),[38] is estimated to be 1.14, 1.32 for Pd/C and electrodeposited Pd NPs, respectively, which is in good agreement with literature.[30-32,39] In the case of Pd/PdCo core-shell catalyst, the poisoning tolerance is 1.76. The considerable enhancement in j_f/j_b for Pd/PdCo core-shell catalyst may be ascribed to the formation of Pd-Co alloy in the outer surface; which is not only very favorable for FA oxidation but also results in a more resistant to the carbonaceous species poisoning such as HCOO and CO.

The long-term stability of the Pd/C, electrodeposited Pd and Pd/PdCo core-shell NPs is examined by chronoamperometry technique for more than 40,000 s as shown in Fig. 6b. The decrease in the mass activity by time could be assigned to the poisoning effects of the species formed during dissociative adsorption of formic acid.[35,38] Moreover, the mass activity drop in the case of Pd/PdCo core-shell catalyst is significantly slower than that of Pd NPs catalyst; i.e. after 40,000 s, the mass activity of Pd/C, electrodeposited Pd NPs and Pd/PdCo core-shell catalysts reach ~11.1, 16.4 and 40.6% of their initial activity, respectively. It should be pointed out that the initial activities of the catalysts are determined at 20 s to avoid the contribution of double-layer discharge and/or hydrogen desorption process.[31,40] Moreover, the final mass activity of Pd/PdCo core-shell catalyst is considerably higher than that of the Pd/C and electrodeposited Pd NPs catalyst. Fig. 6b shows that the Pd/PdCo core-shell catalyst has the better long-term stability for FA electro-oxidation owing to its relatively higher surface area (Table 2) which leads to efficient removal of the intermediate poisonous species.[35]

The polarization and power density curves of a single DFAFC with three catalysts as the anode are shown in Fig. 7a and b. As it is observed, Pd/PdCo catalyst has the highest performance. The maximum power density was approximately 38, 20 and 17 mW cm^{-2} for Pd/PdCo core-shell NPs (Pd load=0.31 mg cm^{-2}), electrodeposited Pd NPs (0.3 mg cm^{-2}) and Pd/C (0.3 mg cm^{-2}) catalyst, respectively. This was a preliminary result and the performance was not very high for DFAFC[40-43] which may be due to the insufficient catalyst loading, low concentration of formic acid and/or no-optimal MEA preparation method. However, the promising point is the power density of Pd/PdCo core-shell NPs catalyst which is ~90% and ~120% higher than those of electrodeposited Pd NPs and Pd/C catalyst.

Figure 7

One of the promotion mechanisms associated with the core-shell nanostructured electrocatalysts can be the consequence of electronic interaction between PdCo shell and Pd core, similar to what reported for the Pd/Pt core-shell nanowires catalyst in the enhanced methanol electro-oxidation process.[44] Since PdCo is less oxophilic than Pd, the removal of intermediates such as CO_{ads} seems to be related to the electron exchange between Pd and PdCo which facilitates the formation of active oxygen species on Pd. However, due to the oxophilic surface of Pd (compared to PdCo),[31] the oxidative removal of CO_{ads} on PdCo shell (CO_{ads} + O_{ads} = CO_2) will be greatly enhanced, if a large number of active oxygen-containing species (e.g.,PdO/PdO_2) are available on the Pd core.[44] The remarkable high mass activity for the FA oxidation reaction on Pd/PdCo core-shell NPs compared to that of Pd NPs electrocatalysts indicates a more effective promoting mechanism for the CO_{ads} removal beyond the promotion described by the general theory of bi-functional catalysts.[45] On the other hand, the well dispersed Pd NPs not only provides an excellent high surface area for the growth of PdCo shell but it also serves as an excellent current collector, another advantage of the Pd/PdCo core-shell NPs compared to the conventional core-shell NPs which require high surface area of a substrate such as carbon as supports and as current collectors.

Conclusions

We described a simple, highly effective method for synthesizing Pd/PdCo core-shell nanoparticles. The mechanisms of the electrochemical nucleation and growth of palladium and cobalt was proposed based on the experimental evidences such as chronoamperometry, EDS, EELS, XRD and XPS. Beside the electrocatalytic activity of synthesized Pd/PdCo core-shell NPs catalyst, which was around 3 and 5 times higher than Pd NPs and Pd/C, the low onset potential and peak potential toward FA oxidation made it as favorable alternative catalysts in DFAFC. The presence of a PdCo alloy shell not only increases the activity of FA oxidation, but also modifies durability and poisoning tolerance of the catalyst due to modified electronic structure of Pd, which we believe is responsible, at least in part, for the higher performance. In addition, the result of single direct formic acid fuel cell using the Pd/PdCo core-shell NPs anode showed higher power density compared with electrodeposited Pd NPs and Pd/C catalysts which can promisingly bring the possibility of commercial exploitation for direct formic acid fuel cells (DFAFCs).

Acknowledgements

This work is a part of project number 92006374 with Iran national science foundation (INSF). The authors appreciate INSF for financial support. The authors wish to thank the renewable energy organization of Iran (SANA) for financial support.

Notes and references

[a]*Laboratory of Advanced Materials for Electrochemical Energy, Department of Mining and Metallurgical Engineering, Amirkabir University of Technology (Tehran Polytechnic), Hafez Ave., P.O. Box 15875-4413, Tehran, Iran. Fax: +98 21 66405846; Tel: +982164542933; E-mail: tabaian@aut.ac.ir*

1. C.Bianchini, P.K.Shen, *Chem. Rev.* 2009, **109**, 4183–4206.

2.M.Rezaei, M.Ghorbani, A.Dolati, *Electrochim. Acta* 2010 **56** 483–490.

3.S.Tominaka, S.Ohta, H.Obata, T.Momma, T.Osaka, *J. Am. Chem. Soc.* 2008, **130**, 10456–10457.

4.S.Tominaka, T.Hayashi, Y.Nakamura, T.Osaka, *J. Mater. Chem.* 2010, **20**, 7175–7182.

5.Y.Suo, L.Zhuang, J.Lu, *Angew. Chem. Int. Ed.* 2007, **46**, 2862–2864.

6.D.Wang, H.L.Xin, H.Wang, Y.Yu, E.Rus, D.A.Muller, F.J.DiSalvo, H.D. Abruña, *Chem. Mater.* 2012, **24**, 2274−2281.

7.L.A.Kibler, A.M.El-Aziz, R.Hoyer, D.M.Kolb, *Angew. Chem. Int. Ed.* 2005, **44**, 2080–2084.

8.J.Jang, C.Pak, Y.Kwon, *J. Power Sources* 2012, **201**, 179–183.

9.J.Yin, S.Shan, M.S.Ng, L.Yang, D.Mott, W.Fang, N.Kang, J.Luo, C.Zhong, *Langmuir* 2013, **XXX**, XXX−XXX.

10.D.J.Ham, C.Pak, G.H.Bae, S.Han, K.Kwon, S.Jin, H.Chang, S.H.Choi, J.S. Lee, *Chem. Commun.* 2011, **47**, 5792–5794.

11.M.H.Shao, T.Huang, P.Liu, J.Zhang, K.Sasaki, M.B.Vukmirovic, R.R. Adzic, *Langmuir* 2006, **22**, 10409–10415.

12.C.Su, F.He, H.Ju, Y.Zhang, E.Wang, *Electrochim. Acta* 2009, **54**, 6257–6263.

13.A.E.Alvarez, D.R. Salinas, *Electrochim. Acta* 2010, **55**, 3714–3720.

14.H.Huang, C.Lin, F.Chen, W.Li, *Electrochim. Acta* 2013, **97**, 244–252.

15.C.Han, Q.Liu, D.G. Ivey, *Electrochim. Acta* 2009, **54**, 3419–3427.

16.A.Milchev, *Russ. J. Electrochem.* 2008, **44**, 619–645.

17.A.Milchev, E.Michailova, T.Zapryanova, *Electrochem. Commun.* 2004, **6**, 713–718.

18.O.Díaz-Morales, J.Mostany, C.Borrás, B.R. Scharifker, *J. Solid State Electrochem.* 2013, **17**, 345–351.

19.C.Cui, L.Gan, M.Heggen, S.Rudi,P. Strasser, *Nat. Mater.* 2013, **12**, 765–771.

20.M.Shao, K.Sasaki, R.R. Adzic, *J. Am. Chem. Soc.* 2006, **128**, 3526–3527.

21.J.Snyder, I.McCue,K. Livi, J.Erlebacher, *J. Am. Chem. Soc.* 2012, **134**, 8633−8645.

22.M. Rezaei, S.H. Tabaian, D.F. Haghshenas, *Electrochim. Acta* 2012, **59**, 360–366.

23.M. Rezaei, S.H. Tabaian, D.F. Haghshenas, *J. Electroanal. Chem.* 2012, **687**, 95–101.

24.M. Rezaei, S.H. Tabaian, D.F. Haghshenas, *Electrochim. Acta* 2013, **87**, 381–387.

25.M. Palomar-Pardave, B.R. Scharifker, E.M. Arce, M. Romero-Romo,*Electrochim. Acta* 2005, **50**, 4736–4745.

26.Y. Surendranath, D.A. Lutterman, Y. Liu, D.G. Nocera, *J. Am. Chem. Soc.* 2012, **134**, 6326−6336.

27.J. Ustarroz, J.A. Hammons, T. Altantzis, A. Hubin, S. Bals, H. Terryn, *J. Am. Chem. Soc.* 2013, **135**, 11550−11561.

28.J.F. Moulder, W.F. Stickle, P.E. Sobol,K.D. Bomben, *Handbook of X-ray Photoelectron Spectroscopy*, Physical Electronics, Inc., Minnesota, USA, 1992.

29.R. Ahmadi, M.K. Amini, J.C. Bennett, *J. Catalysis* 2012, **292**, 81–89.

30.R. Li, Z. Wei, T. Huang, A. Yu, *Electrochim. Acta* 2011, **56**, 6860–6865.

31.L. Zhang, L. Wan, Y. Ma, Y. Chen, Y. Zhou, Y. Tang, T. Lu, *Appl. Catal. B: Environ.* 2013, **138–139**, 229–235.

32 C. Hsu, C. Huang, Y. Hao, F. Liu, *Electrochem. Commun.* 2012, **23**, 133–136.

33.B. Hammer, J.K. Nørskov, *Adv. Catal.* 2000, **45**, 71–129.

34.X. Ji, K.T. Lee, R. Holden, L. Zhang, J. Zhang, G.A. Botton, M. Couillard, L.F. Nazar, *Nat. Chem.* 2010, **553**, 286–293.

35.S. Zhang, S. Guo, H. Zhu, D. Su, S. Sun, *J. Am. Chem. Soc.* 2012, **134**, 5060−5063.

36.V.R. Stamenkovic, B.S. Mun, M. Arenz, K.J.J. Mayrhofer, C.A. Lucas, G. Wang, P.N. Ross, N.M. Markovic, *Nat. Mater.* 2007, **6**, 241–247.

37.V.R. Stamenkovic, B. Fowler, B.S. Mun, G. Wang, P.N. Ross, C.A. Lucas, N.M. Markovic, *Science* 2007, **315**, 493–497.

38.L. Liu, E. Pippel, R. Scholz, U. Gosele, *Nano Lett.* 2009, **9**, 4352–4358.

39.N. Cheng, H. Lv, W. Wang, S. Mu, M. Pan, F. Marken, *J. Power Sources* 2010, **195**, 7246–7249.

40.N. Fujiwara, Z. Siroma, T. Ioroi, K. Yasuda, *J. Power Sources* 2007, **164**, 457–463.

41.R.D. Morgan, J.L. Haan, R.I. Masel, *J. Power Sources*2010, **195**, 6405–6410.

42. J.Yeom, R.S. Jayashree, C. Rastogi, M.A. Shannon, P.J.A. Kenis, *J. Power Sources*2006, **160**, 1058–1064.

43.L. Feng, L. Yan, Z. Cui, C. Liu, W. Xing, *J. Power Sources*2011, **196**, 2469–2474.

44.H. Wang, C. Xu, F. Cheng, M. Zhang, S. Wang, S.P. Jiang,*Electrochem. Commun.* 2008, **10**, 1575–1578.

45.Y.H. Wen, R. Huang, C. Li, Z.Z. Zhu, S.G. Sun, *J. Mat. Chem.* 2012, **22**, 7380–7386.

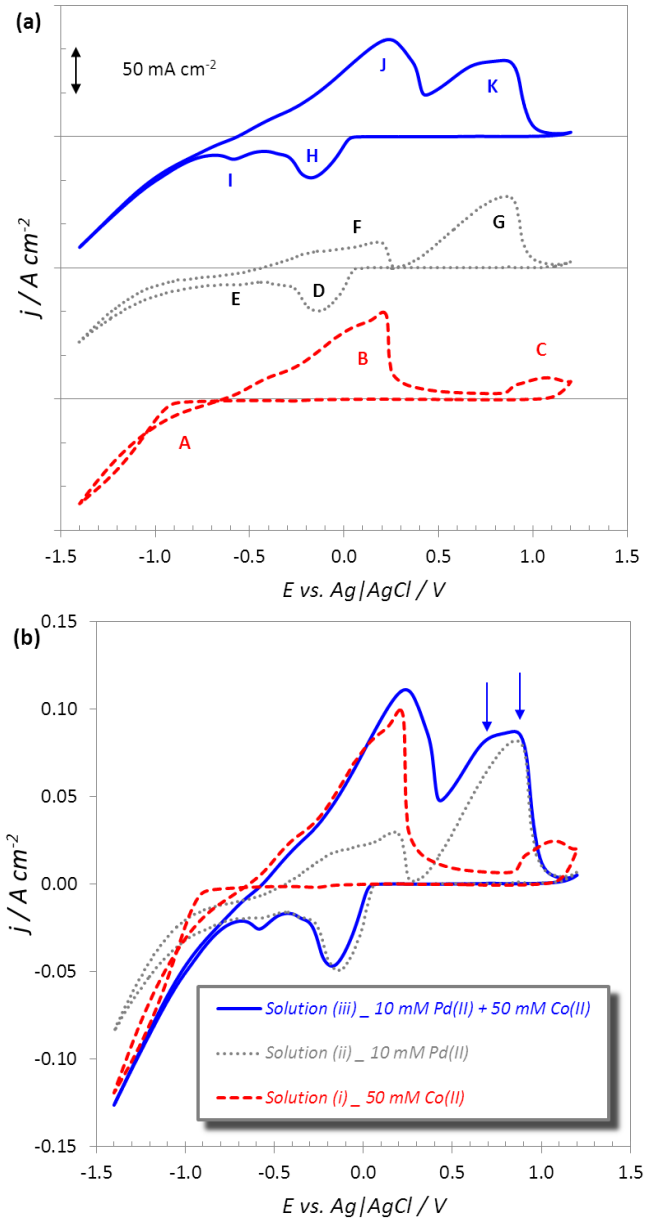

Figure 1. Cyclic voltammograms of carbon cloth electrode in solutions contain 1 M NH_4Cl as the electrolyte supporting and i) 50 mM $CoSO_4$ (pH=3.5), ii) 10 mM $PdCl_2$ (pH=3.4) and iii) 10 mM $PdCl_2$ + 50 mM $CoSO_4$ (pH=3.2). (a) the distinctive and (b) the collective voltammograms.

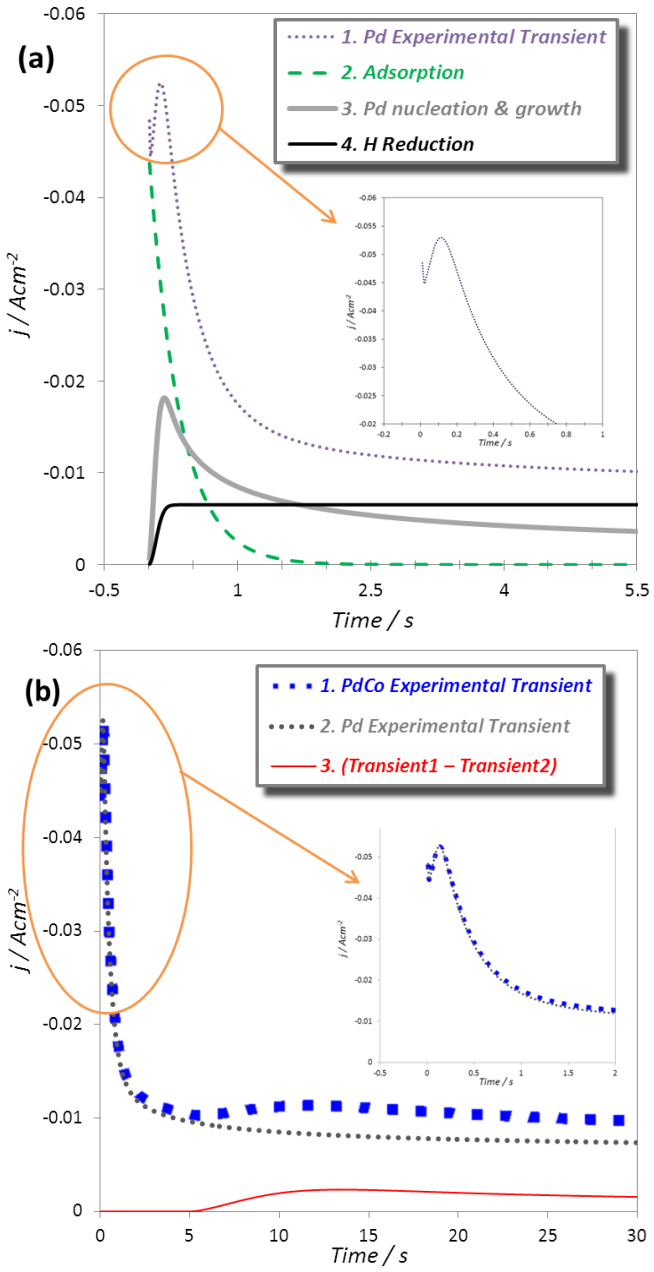

Figure 2. (a) Current transient of carbon cloth in solution: (1 M NH_4Cl + 10 mM $PdCl_2$) at E=–1.2 V and the nonlinear fitted curves according to Eq. (1) corresponding to adsorption, hydrogen reduction as well as the palladium 3D nucleation and diffusion controlled growth. (b) The comparison of the transients of carbon cloth in solution (1 M NH_4Cl + 10 mM $PdCl_2$) and (1 M NH_4Cl + 10 mM $PdCl_2$ + 50 mM $CoSO_4$) as well as the subtraction of these two transients which initiates after t=5.1 s.

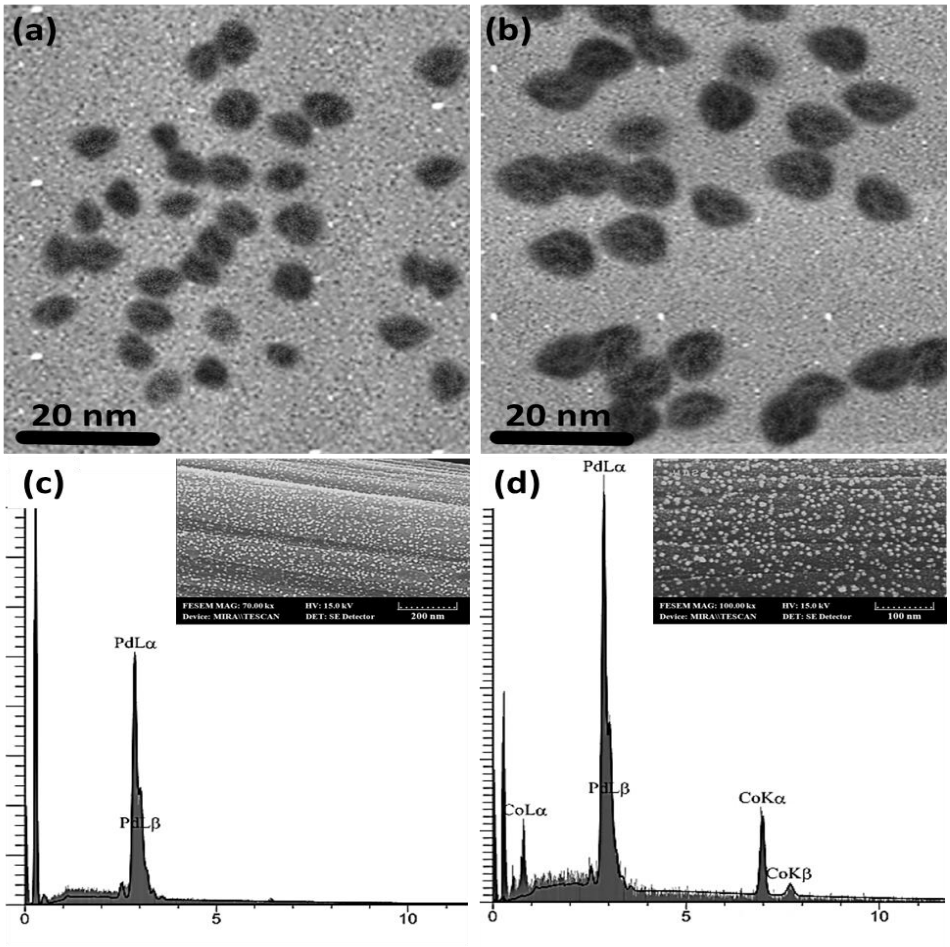

Figure 3. (a,c) TEM and FESEM micrographs as well as the EDS spectrum of the Pd NPs electrodeposited in solution: (1 M NH_4Cl + 10 mM $PdCl_2$ + 50 mM $CoSO_4$) with the deposition time 4 seconds. (b,d) micrographs and EDS spectrum of the Pd/PdCo core-shell NPs electrodeposited in the same solution with the deposition time of 15 seconds.

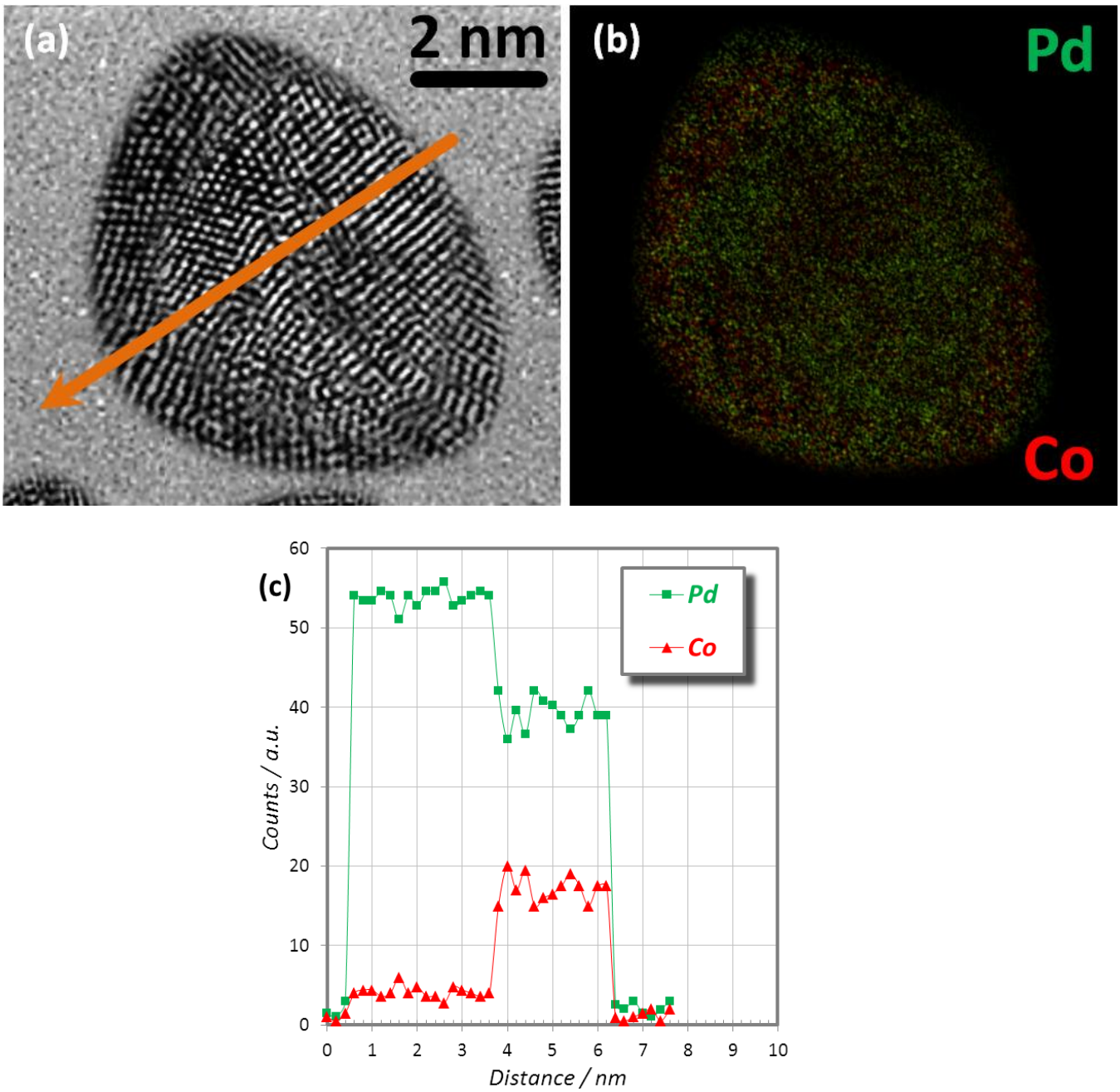

Figure 4. (a) HRTEM micrograph of the Pd/PdCo core-shell NP electrodeposited in solution: (1 M NH_4Cl + 10 mM $PdCl_2$ + 50 mM $CoSO_4$) at E=–1.2 V with the deposition time 15 seconds. (b) the EELS color elemental-map of the Pd/PdCo core-shell NP shown in Figure 4(a) and (c) the EELS line profile scanned on the arrow shown in Figure 4(a) for palladium and cobalt elements.

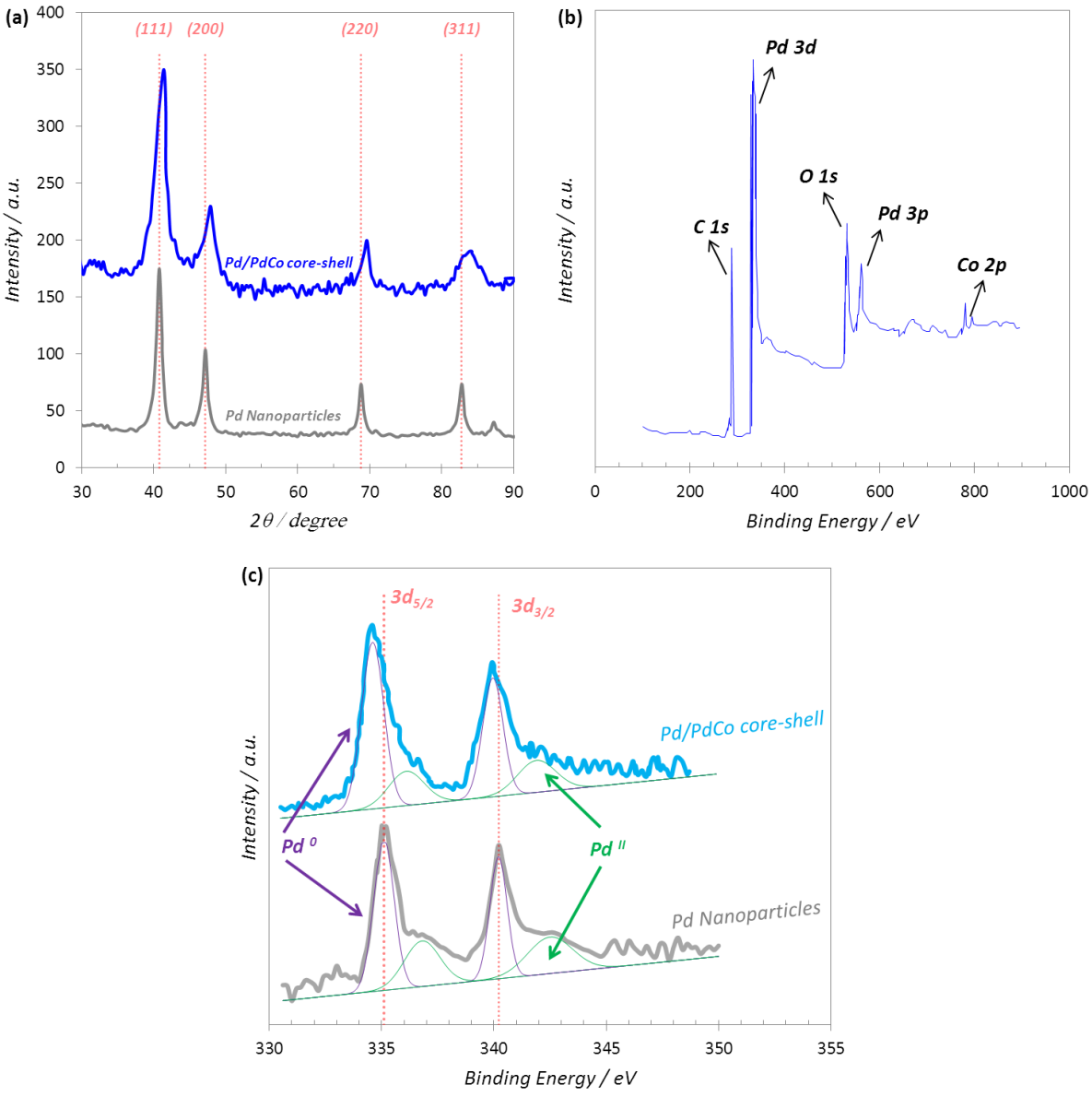

Figure 5. (a) The X-ray diffraction pattern of electrodeposited Pd NPs and Pd/PdCo core-shell NPs as well as the standard peak positions of face center cubic (fcc) palladium (dash vertical lines), (b) Survey scan XPS spectrum of Pd/PdCo core-shell NPs in region from 100 - 900 eV and (c) the high resolution spectra for Pd 3d region for both Pd NPs (deposition time = 4 s in 1 M NH_4Cl + 10 mM $PdCl_2$ + 50 mM $CoSO_4$) and Pd/PdCo core-shell NPs (deposition time = 15 s in the same solution).

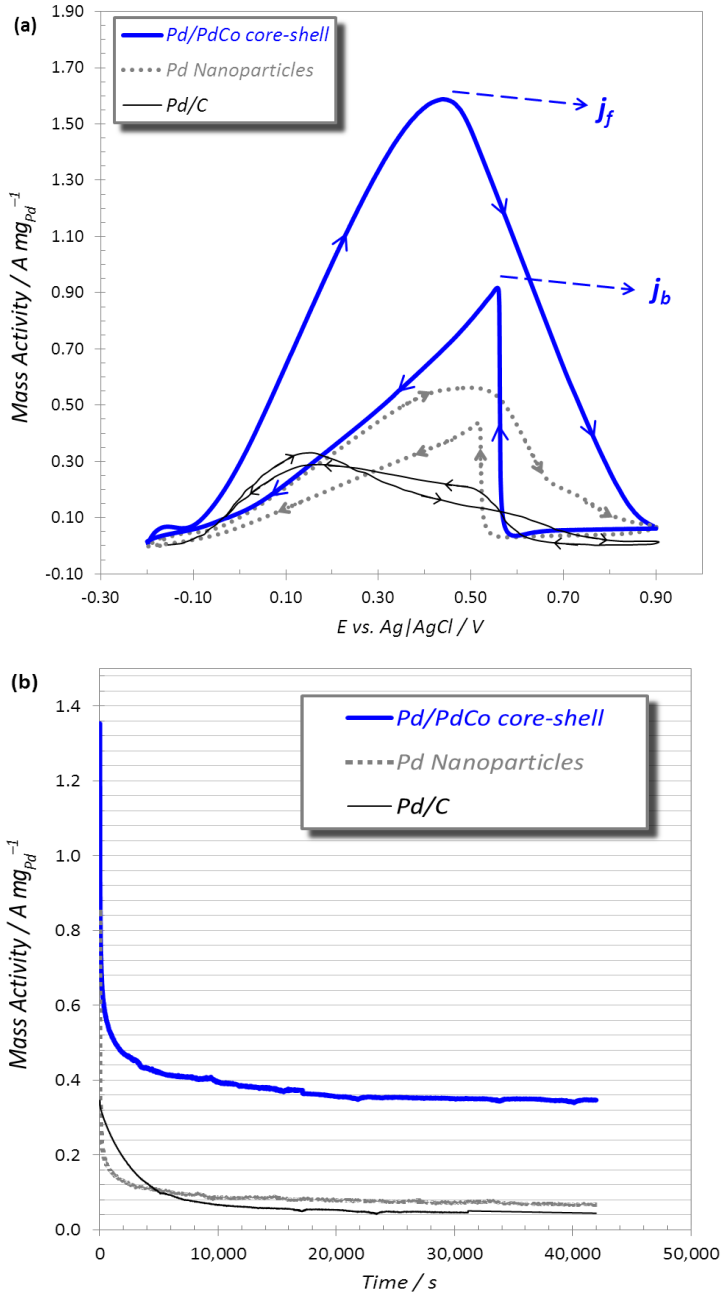

Figure 6. (a) Cyclic voltammetry curves of Pd/C, electrodeposited Pd NPs and Pd/PdCo core-shell NPs in 0.5 M HCOOH + 0.5 H_2SO_4 and (b) long-time chronoamperometry curves of the same catalysts in the same solution for 12 hours.

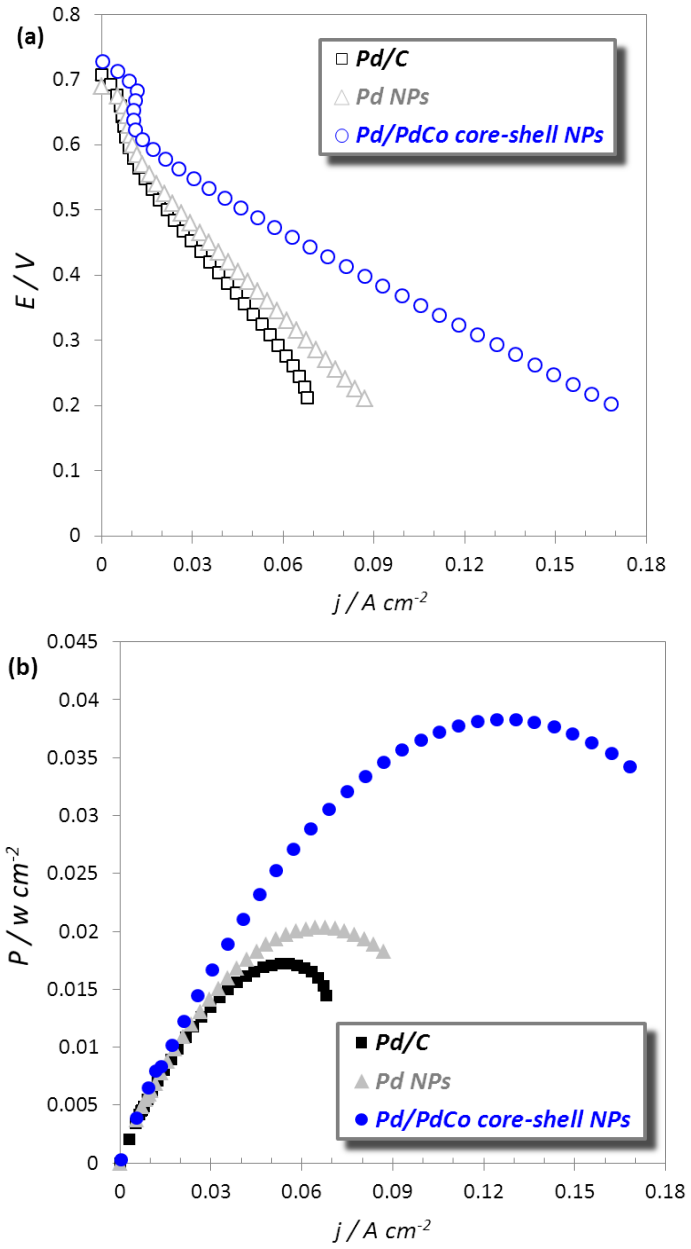

Figure 7. (a) The polarization curve of single direct formic acid fuel cell with the three anode catalyst: commercial Pd/C (20 wt.%), electrodeposited Pd NPs and Pd/PdCo core-shell NPs with the Pd loading of ≃0.30, 0.30, 0.31 mg cm^{-2}. The cathode catalyst is commercial 0.2 mg cm^{-2} of Pt/C (10 wt. %) and the membrane is Nafion 115 (DuPont Inc.). The flow of fuel is 1 ml min^{-1} with the formic acid concentration of 0.5 M and 50 sccm of dry air. The active surface of the mono cell was 5 cm^2 and the cell operated at ambient temperature and pressure. (b) The curve of power density versus current density derived from Fig. 7a.